

## Modeling spreading with degassing using anisotherm viscoplastic multiphase shallow water approximation

Thomas Schiano <sup>a,b</sup>, Barbara Bigot <sup>a,\*</sup>, Jean-François Haquet <sup>a</sup>, Pierre Saramito <sup>b</sup>, Claude Smutek <sup>c</sup>

<sup>a</sup> CEA, DES, IRESNE, DTN, SMTA, LMAG, Cadarache, F-13108 St Paul Lez Durance, France

<sup>b</sup> Laboratoire Jean Kuntzmann, Grenoble-Alpes University, 700 Avenue Centrale, 38400 Saint Martin d'Hères, France

<sup>c</sup> Laboratoire GéoSciences Réunion, Réunion University, Institut de Physique du Globe de Paris, Sorbonne Paris-Cité, 15 av. René Cassin, 97400 Saint-Denis, France

### ARTICLE INFO

#### Keywords:

Spreading  
Free-surface  
Shallow water  
Degassing  
Phase field  
Modeling  
Numerical simulation

### ABSTRACT

During a nuclear reactor severe accident such as those of Three Mile Island, Chernobyl or Fukushima, it is crucial to contain the radiological consequences to the power plant. A severe accident of a Pressurized Water Reactor (PWR) occurs when the nuclear fuel, in case of loss of cooling, melts and mixes with the core structures (assemblies and internal structures) to form a high temperature ( $\sim 3000$  K) and density magma so-called corium. Several strategies are studied to cool the corium and to limit its propagation in the power plant in order to avoid the outside contamination. The Ex-Vessel Retention (EVR) strategy consists in spreading the corium on a basemat to promote its cooling and prevent basemat significant ablation by increasing the corium cooling surface and thus reducing the thermal load on the reactor structure. This paper is dedicated to tridimensional modeling corium spreading with gas released from a substrate using an anisotherm viscoplastic multiphase shallow water approximation. It is reduced to an height-averaged bidimensional model and its use for molten nuclear core spreading is argued with dimensionless numbers. Using an adaptive finite element method based on C++ library Rheolef, simulations are ran. A sensitivity analysis on the numerical parameters and the gas inflow rate are conducted. Tridimensional solution of the problem is computed from the bidimensional height-averaged solution.

### 1. Introduction

High density and temperature fluid spreading is an issue met in many situations such as volcanic lava flows (Roult et al., 2012; Vileneuve et al., 2008) and nuclear severe accidents (Weisshäupl, 1999; Journeau et al., 2003). These are described by complex multiphase flows characterized by coupled multi-physics phenomena such as solidification due to heat transfers (at the surface by radiation or by convection in the presence of water, with the substrate by conduction), the rheology of the fluid (possibly non Newtonian) or interactions with the substrate (ablation, degassing). A viscoplastic (non Newtonian) description of corium has been gathering interest since the viscosity and yield stress measurements made by Roche et al. (1994). They lead us to consider a greater range of fluid behavior. Fig. 1 presents the stress tensor according to the deformation rate tensor and allows illustrating the different behaviors of a fluid according to the Herschel and Bulkley (1926) viscoplastic model that depends on two parameters: the fluid index,  $n$ , and yield stress,  $\tau_y$ . For  $n = 1$  and  $\tau_y = 0$ , this fluid is considered as Newtonian, for  $n = 1$  and  $\tau_y \neq 0$  as viscoplastic Binghamian (Bingham, 1922), and for  $n \neq 1$  and  $\tau_y \neq 0$  as general viscoplastic.

As pointed out by Saramito and Wachs (2017), the regularization approach currently used in industrial codes lacks a general convergence result of the solution with the regularization parameter and cannot follow the unyielded regions of a yield stress fluid flow with the deformation rate tensor  $\dot{\gamma} = 0$ .

The use of asymptotic analysis to provide shallow approximations for free surface viscoplastic flows has been introduced by Liu and Mei (1989) and further experimental and mathematical analysis was performed by Balmforth et al. (2007). Spread over an arbitrary topography was studied by Bernabeu et al. (2014). Adding thermal effects has shown to be more complex as the energy equation does not reduce to a bidimensional one using the asymptotic analysis approach. Bercovici and Lin investigated this particular issue for Newtonian fluids in Bercovici and Lin (1996) and Balmforth et al. (2004) built upon it to propose a model with temperature-dependent consistency and temperature-independent yield stress for shallow viscoplastic flows. Then, Bernabeu et al. (2016) proposed a model with height-averaged temperature-dependent consistency and yield-stress comparing second and third order polynomial vertical distribution of temperature.

\* Corresponding author.

E-mail address: [barbara.bigot@cea.fr](mailto:barbara.bigot@cea.fr) (B. Bigot).

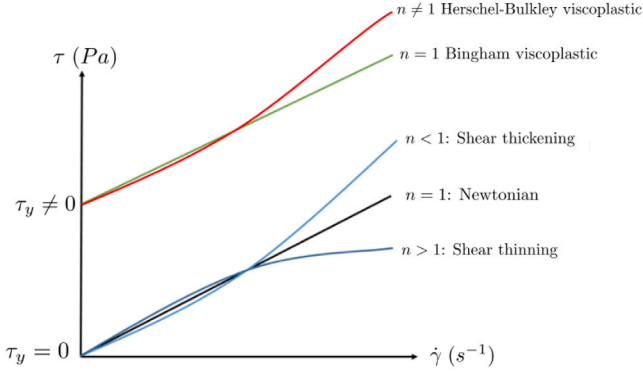


Fig. 1. Stress tensor according to deformation rate tensor illustrating the different behaviors of a fluid according to the Herschel–Bulkley model with two parameters: the fluid index,  $n$ , and yield stress,  $\tau_y$ . For  $n = 1$  and  $\tau_y = 0$ , fluid is considered as Newtonian, for  $n = 1$  and  $\tau_y \neq 0$  as Binghamian, and for  $n \neq 1$  as viscoplastic.

Here, we propose to adapt this latter viscoplastic model (Bernabeu et al., 2016) to shallow anisotherm multiphase spreading with a second-order temperature polynomial approximation with non-constant viscosity using a model based on Shaw law (Shaw, 1969) and first-order volume fraction polynomial approximation.

To account for the effect of degassing, we base our method on the phase field method which has been introduced by Cahn and Hilliard (1958) then enhanced in Allen and Cahn (1979). We use a mixture model as described in Damián and Nigro (2014), Meng et al. (2022), using relative velocity models from the works of Ishii (1977), Ishii and Zuber (1979), Hibiki and Ishii (2003) and the continuum surface force model by Brackbill et al. (1992).

We first present the tridimensional model, then perform a dimensional analysis on it before giving its reduced form by expanding on the process provided by Bernabeu et al. (2016). Then, using the C++ library (Saramito, 2019), sensitivity analysis is performed on numerical parameters and gas inflow velocity. Finally, we discuss the tridimensional reconstructed results.

## 2. Mathematical model

In this section, we present the multiphase viscoplastic model. Fig. 2 shows the spreading scheme with the melt spread. It involves three domains, denoted by the indices  $f$ ,  $s$  and  $ext$  that represent respectively the melt, the substrate and the ambient environment of the spread. Let  $Q$ , the whole domain, be an open set of  $\mathbb{R}^3$  of regular border  $\partial Q$ . It splits as  $Q = Q_f(t) \cup Q_s$  where  $Q_f(t)$  is the melt flow region, and  $Q_s$  the substrate. The boundary of the melt flow region also splits as  $\partial Q_f(t) = \Gamma_f(t) \cup \Gamma_s \cup \Gamma_w$  where  $\Gamma_f(t)$  is the free surface of the flow,  $\Gamma_s$  the horizontal plane where the melt is in contact with the substrate where degassing happens and  $\Gamma_w$  the vertical walls. Finally, a part  $\Gamma_e \subset \Gamma_s$  corresponds to the melt alimentation region, where there is an inflow.

### 2.1. Tridimensional mixture model

We use the phase field method equation used by Chiu (2011), replacing the curvature proportional term by a relative velocity dependent one in order to track the volume fraction of the melt  $\phi$ , such as:

$$\partial_t \phi + \mathbf{u} \cdot \nabla \phi + \nabla \cdot (\phi(1 - \phi)\mathbf{w}) = 0 \quad (1a)$$

where  $\mathbf{u} = \phi \mathbf{u}_1 + (1 - \phi) \mathbf{u}_2$  is the volumetric mixture velocity with  $\mathbf{u}_1$  and  $\mathbf{u}_2$  respectively the continuous phase velocity and dispersed phase velocity (e.g.) the velocity of the liquid and vapor phases) and  $\mathbf{w} = \mathbf{u}_1 - \mathbf{u}_2$  is the relative velocity between phases, following the model

from Damián and Nigro (2014), we model it by neglecting relative velocity along the  $x$  and  $y$  directions with a constitutive law:

$$w_z = w_s \phi(1 - \phi) \quad (1b)$$

the  $w_s$  constant can be interpreted as in Damián and Nigro (2014) by the terminal velocity of a single bubble moving in a continuous phase and we can determine it using the drag laws provided by Hibiki and Ishii in Hibiki and Ishii (2003) for bubbly flows from which we use  $w_s = \sqrt{2} \left( \frac{|\sigma_{cap}(\rho_1 - \rho_2)|}{\rho_1} \right)^{1/4}$ , with  $\rho_1$  and  $\rho_2$  the density of media 1 and 2 and  $\sigma_{cap}$  the surface tension. This assumption is justified for our application in section 3.

We model the two phases using a mixture model that uses the Herschel–Bulkley constitutive equation, which expresses the deviatoric part  $\boldsymbol{\tau}$  of the Cauchy stress tensor in the melt as

$$\begin{cases} \boldsymbol{\tau} = \left( K(\theta, \phi) \dot{\boldsymbol{\gamma}}^{n-1} + \frac{\tau_y(\theta, \phi)}{|\dot{\boldsymbol{\gamma}}|} \right) \dot{\boldsymbol{\gamma}} & \text{when } \dot{\boldsymbol{\gamma}} \neq 0, \\ |\boldsymbol{\tau}| \leq \tau_y(\theta, \phi) & \text{otherwise,} \end{cases} \quad (1c)$$

where  $\dot{\boldsymbol{\gamma}} = \nabla \mathbf{u} + \nabla \mathbf{u}^T$  is the shear rate tensor and  $\theta$  is the temperature. Also  $K(\theta, \phi)$  is the temperature and volume fraction-dependent consistency index,  $\tau_y(\theta, \phi)$ , the temperature-dependent yield stress and  $n$  is the power-law index. As depicted on Fig. 1, for  $\tau_y = 0$  and  $n = 1$ , the fluid is Newtonian, and  $K(\theta, \phi)$  is the temperature and volume fraction-dependent viscosity. Here, the temperature dependence of both consistency index and yield stress follow the Shaw model with the same coefficient (Shaw, 1969):

$$\begin{aligned} K(\theta, \phi) &= \phi K_e \exp \left( Arr \left( \frac{\theta_e - \theta}{\theta_e - \theta_a} \right) \right) + (1 - \phi) K_2 \\ \tau_y(\theta, \phi) &= \phi \tau_{y,e} \exp \left( Arr \left( \frac{\theta_e - \theta}{\theta_e - \theta_a} \right) \right) \end{aligned}$$

with  $K_e$  and  $\tau_{y,e}$ , the value of  $K(\theta, \phi)$  and  $\tau_y(\theta, \phi)$  at the inlet reference temperature  $\theta_e$  and with  $\phi = 1$ . The values of the constants  $\tau_{y,e}$ ,  $K_e$  and  $Arr$  are determined through the viscosity and yield stress measurements of Roche et al. (1994) and Ramacciotti et al. (2001) for the application in this article.  $K_2$  is the value of  $K(\theta, \phi)$  for  $\phi = 0$ . Assuming a constant density for both phases for the continuous phase and the dispersed phase and a mixture density of  $\rho(\phi) = \phi \rho_1 + (1 - \phi) \rho_2$ , the mass conservation equation of the mixture yields:

$$\nabla \cdot \mathbf{u} = 0 \quad (1d)$$

and using the continuum surface force (CSF) model by Brackbill et al. (1992), the momentum conservation equation becomes :

$$\partial_t(\rho(\phi)\mathbf{u}) + \nabla \cdot (\rho(\phi)\mathbf{u} \otimes \mathbf{u}) = \nabla \cdot (-p\mathbb{I} + \boldsymbol{\tau}) - \sigma_{cap} \nabla \cdot \left( \frac{\nabla \phi}{|\nabla \phi|} \right) \nabla \phi + \rho(\phi)\mathbf{g} \quad (1e)$$

where  $p$  is the pressure and  $\mathbf{g}$  the gravity vector. The energy conservation equation reads:

$$c_p(\partial_t(\theta\rho(\phi)) + \mathbf{u} \cdot \nabla \theta\rho(\phi)) - \nabla \cdot (k(\phi)\nabla \theta) = 0 \quad (1f)$$

with  $c_p$  the specific heat capacity and  $k$  the volume fraction-dependent heat conduction coefficient, with  $k(\phi) = \phi k_e + (1 - \phi)k_2$ ,  $k_e$  its value for the first phase and  $k_2$  its value for the second one. As in Bernabeu et al. (2016) and Schiano et al. (2023), we neglect the friction dissipation term and temperature-driven buoyancy. Considering the substrate  $Q_s$  as a rigid solid that is not ablated, the energy conservation equation in the substrate is:

$$\rho_s c_{ps} \partial_t \theta - \nabla \cdot (k_s \nabla \theta) = 0 \quad (1g)$$

where  $\rho_s$  is the density of the substrate,  $c_{ps}$  its specific heat capacity, and  $k_s$  its heat conduction coefficient. Finally, we close the set of Eqs. (1c)–(1g) with initial and boundary conditions. We assume that the free surface  $\Gamma_f(t)$  can be explicitly described by the mixture height function  $h$  by:

$$\Gamma_f(t) = \{(x, y, z) \in \mathbb{R}^3 ; z = h(t, x, y)\}$$

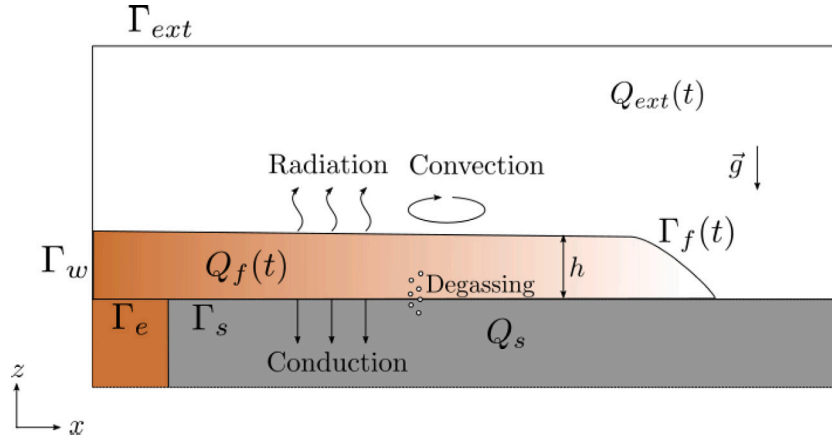


Fig. 2. Multiphase spreading: its geometry and notations.

where, by convention, the plane  $z = 0$  coincides with the melt-substrate interface  $\Gamma_s$ , see Fig. 2. Note that the height  $h(t, x, y)$  is defined for all  $t > 0$  and  $(x, y) \in \Gamma_s \cup \Gamma_e$ . We introduce a level set function  $\varphi_h = z - h(t, x, y)$ , such that  $\varphi_h = 0$  is exactly the free surface. It is transported by the flow:  $\partial_t \varphi_h + \mathbf{u} \cdot \nabla \varphi_h = 0$ . Then, the transport of the free surface by the flow writes:

$$\partial_t h + u_x \partial_x h + u_y \partial_y h - u_z = 0 \quad (1h)$$

The initial conditions on velocity, height, temperature and volume fraction read:

$$\mathbf{u}(t=0) = \mathbf{u}_0 \text{ in } Q_f(t=0) \quad (1i)$$

$$h(t=0) = h_0 \text{ on } \Gamma_s \quad (1j)$$

$$\theta(t=0) = \theta_0 \text{ in } Q_f(t=0) \cup \Gamma_s \cup Q_s \quad (1k)$$

$$\phi(t=0) = \phi_0 \text{ in } Q_f(t=0) \cup \Gamma_s \cup Q_s \quad (1l)$$

where  $\mathbf{u}_0$ ,  $h_0$ ,  $\theta_0$  and  $\phi_0$  are known from experimental measurements. In the following study, they correspond to  $h_0 = 0$ ,  $\mathbf{u}_0 = 0$ ,  $\theta_0 = \theta_a$ , the atmospheric temperature and  $\phi_0 = 0$ . A Dirichlet condition for velocity on the substrate plane  $\Gamma_s$  and the inlet plane  $\Gamma_e$  is used, as they are considered as no-slip boundaries. It is completed with the inlet velocity condition for the  $z$ -component:

$$u_x = u_y = 0 \text{ and } u_z = w_e \text{ on } (\Gamma_e \cup \Gamma_s) \cap \partial Q_f(t) \quad (1m)$$

where  $w_e$  is the inlet velocity, which is deduced from the measured flow rate for the region  $\Gamma_e \cap \partial Q_f(t)$  and from the degassing flow rate for the substrate contact region  $\Gamma_s \cap \partial Q_f(t)$ . On the vertical walls  $\Gamma_w$ , the no-slip boundary condition simply becomes  $\mathbf{u} = 0$ . On the free surface  $\Gamma_f(t)$ , surface tension effects are neglected, so the normal Cauchy stress is just zero, i.e.:

$$(\boldsymbol{\tau} - p\mathbf{I}) \cdot \mathbf{n} = 0 \text{ on } \Gamma_f(t) \quad (1n)$$

where  $\mathbf{n}$  denotes the outward unit normal at  $Q_f(t)$  on the free surface  $\Gamma_f(t)$ . A Dirichlet condition for temperature on  $\Gamma_s$  is given to model inlet temperature in its inlet region  $\Gamma_e$ :

$$\theta = \theta_e \text{ on } \Gamma_e \quad (1o)$$

On  $\Gamma_s$  but outside of this inlet region  $\Gamma_e$ , the melt is in contact with the substrate: the temperature is continuous across  $\Gamma_s$  while the heat transfer is considered to be dominantly conductive:

$$\theta|_{Q_f} = \theta|_{Q_s} \text{ on } \Gamma_s \setminus \Gamma_e \quad (1p)$$

$$k \mathbf{n} \cdot \nabla(\theta|_{Q_f}) = k_s \mathbf{n} \cdot \nabla(\theta|_{Q_s}) \text{ on } \Gamma_s \setminus \Gamma_e \quad (1q)$$

where  $\theta|_{Q_f}$  (resp.  $\theta|_{Q_s}$ ) denotes the restriction of the temperature  $\theta$  in the melt (resp. substrate) region and  $\mathbf{n}$  is the outward unit normal

at  $Q_f(t)$  on the substrate plane  $\Gamma_s$ . On the free surface  $\Gamma_f(t)$ , both radiative and convective heat transfers with the environment are taken into account:

$$k \mathbf{n} \cdot \nabla \theta + \epsilon \sigma_{SB} (\theta^4 - \theta_a^4) + \lambda (\theta - \theta_a) = 0 \text{ on } \Gamma_f(t) \quad (1r)$$

with  $\epsilon$  is the emissivity,  $\sigma_{SB}$ , the Stefan–Boltzmann constant and  $\lambda$ , the convective heat transfer coefficient. Finally, the temperature at the bottom of the substrate is assumed to tend to the atmospheric one:

$$\theta(z = -\infty) = \theta_a. \quad (1s)$$

A Dirichlet condition for volume fraction is given on  $\Gamma_s$  and  $\Gamma_e$ , presuming that each border can release only one type of phase:

$$\phi = 1 \text{ on } \Gamma_e \quad (1t)$$

$$\phi = 0 \text{ on } \Gamma_s \quad (1u)$$

The set of Eqs. (1c)–(1u) defines the tridimensional multiphase viscoplastic melt spreading problem with six unknowns ( $\boldsymbol{\tau}$ ,  $\mathbf{u}$ ,  $p$ ,  $h$ ,  $\theta$ ,  $\phi$ ) that is time and space-dependent, while the computational space is time-dependent since it involves a free-surface.

## 2.2. Dimensional analysis

In 2013, Bernabeu et al. (2014) has shown that the tridimensional isothermal viscoplastic free-surface problem could be reduced as a bidimensional one in terms of the height  $h$  only as unknown. This reduction bases on a dimensional and asymptotic analysis, assuming that the aspect ratio of the height versus the horizontal length is small. This result was extended in 2016 in Bernabeu et al. (2016) for anisotherm viscoplastic free-surface flows, with the height  $h$  and the height-averaged temperature  $\bar{\theta}$  as unknowns. We define the height average  $\bar{\xi}$  of any quantity  $\xi$  by:

$$\bar{\xi}(t, x, y) = \begin{cases} \frac{1}{h(t, x, y)} \int_0^{h(t, x, y)} \xi(t, x, y, z) dz & \text{when } h(t, x, y) \neq 0 \\ 0 & \text{otherwise} \end{cases}$$

Here we perform the same reduction process for tridimensional anisotherm multiphase viscoplastic free-surface flows. We neglect the effect of temperature and volume fraction vertical variation on density, consistency index, yield stress and heat conduction coefficient, so they depend only on the vertical averaged temperature and volume fraction:  $\rho(\phi) = \rho(\bar{\phi})$ ,  $K(\theta, \phi) = K(\bar{\theta}, \bar{\phi})$ ,  $\tau_y(\theta, \phi) = \tau_y(\bar{\theta}, \bar{\phi})$  and  $k(\phi) = k(\bar{\phi})$ . The problem is rewritten using dimensionless quantities and unknowns that are compared in order to simplify it using physical arguments. Those dimensionless unknowns are denoted with tildes. Let  $H$  be the

characteristic flow height and  $L$  its characteristic horizontal length, we introduce the aspect ratio:

$$\varepsilon = \frac{H}{L}.$$

Temperature is written as  $\theta = \bar{\theta}(\theta_e - \theta_a) + \theta_a$ , volume fraction is already dimensionless. Hence density, consistency index, yield stress and heat conduction coefficient are expressed as  $\rho(\phi) = \rho_1 \bar{\rho}(\bar{\phi})$ ,  $K(\theta, \phi) = K_e K(\bar{\theta}, \bar{\phi})$  and  $\tau_y(\theta, \phi) = \tau_{y,e} \bar{\tau}_y(\bar{\theta}, \bar{\phi})$ ,  $k(\phi) = k_e k(\bar{\phi})$  with  $\rho_e = \rho(\bar{\phi} = 1)$ ,  $K_e = K(\bar{\theta} = 1, \bar{\phi} = 1)$ ,  $\tau_{y,e} = \tau_y(\bar{\theta} = 1, \bar{\phi} = 1)$  and  $k_e = k(\bar{\phi} = 1)$ . Horizontal velocity scaling is taken from viscous gravity balance as in Huppert (1982) and Bernabeu et al. (2014):

$$U = \left( \frac{\rho_e g H^2}{K_e L} \right)^{1/n} H$$

and the vertical velocity scaling is  $W = \varepsilon U$ . A characteristic viscosity is also given in Huppert (1982),  $\eta = K_e (U/H)^{n-1}$ . We also consider the time scale  $t = T\bar{t}$  with  $T = \frac{L}{U}$  and the pressure scale  $p = P\bar{p}$  with  $P = \rho_e g H$ . Using the variable change:

$$x = L\bar{x}, \quad y = L\bar{y}, \quad z = H\bar{z}, \quad h = H\bar{h}, \quad u_x = U\bar{u}_x, \quad u_y = U\bar{u}_y, \quad u_z = W\bar{u}_z,$$

we rewrite the set of Eqs. (1c)–(1u) in a dimensionless manner, omitting the tildes thereafter.

### 2.2.1. Dimensionless constitutive equation

Following the work in Bernabeu et al. (2014), we introduce the Bingham number  $Bi$ :

$$Bi = \frac{\tau_{y,e} H}{\eta U},$$

and we give the non-dimensional version of Herschel–Bulkley constitutive Eq. (1c):

$$\begin{cases} \tau_{ij} = \left( \frac{B(\theta, \phi)}{\varepsilon |\dot{\gamma}|} + \varepsilon |\dot{\gamma}|^{n-1} \right) \dot{\gamma}_{ij} \\ \varepsilon |\tau| < Bi \end{cases} \quad (2a)$$

with  $B(\theta, \phi) = Bi \tau_y(\theta, \phi)$ .

### 2.2.2. Dimensionless conservation equations

To write the dimensionless conservation equations, the dimensionless quantities related to transient and advection terms are set equal to 1. Consequently, each volumic and surfacic term in the right side of these equations is multiplied by  $L/(\rho U^2)$ . The dimensionless mass conservation Eq. (1d) becomes:

$$\nabla \cdot \mathbf{u} = 0 \quad (2b)$$

Introducing the Reynolds  $Re$ , Froude  $Fr$  and Weber  $We$  numbers:

$$Re = \frac{\rho_e U L}{K_e},$$

$$Fr = \frac{U}{\sqrt{gL}},$$

$$We = \frac{\rho_e U^2 L}{\sigma_{cap}},$$

the momentum conservation equation along  $x_i$ -axis with  $i \in \{x, y\}$  becomes:

$$\begin{aligned} (\partial_t(\rho(\phi)u_i) + u_x \partial_x(\rho(\phi)u_i) + u_y \partial_y(\rho(\phi)u_i) + u_z \partial_z(\rho(\phi)u_i)) = & -\frac{1}{Fr^2} \partial_i p \\ & + \frac{1}{Re} \left( \partial_x \tau_{ix} + \partial_y \tau_{iy} + \frac{1}{\varepsilon^2} \partial_z \tau_{iz} \right) + \frac{1}{\varepsilon We} \left( -\nabla \cdot \frac{\nabla \phi}{|\nabla \phi|} \right) \partial_i \phi, \end{aligned} \quad (2c)$$

and the momentum equation along  $z$ -axis is:

$$\begin{aligned} (\partial_t(\rho(\phi)u_z) + u_x \partial_x(\rho(\phi)u_z) + u_y \partial_y(\rho(\phi)u_z) + u_z \partial_z(\rho(\phi)u_z)) \\ = \frac{1}{\varepsilon^2 Fr^2} \left( \frac{g}{|g|} \rho(\phi) - \partial_z p \right) \end{aligned}$$

$$+ \frac{1}{\varepsilon^2 Re} (\partial_x \tau_{zx} + \partial_y \tau_{zy} + \partial_z \tau_{zz}) + \frac{1}{\varepsilon^3 We} \left( -\nabla \cdot \frac{\nabla \phi}{|\nabla \phi|} \right) \partial_z \phi \quad (2d)$$

Using the Peclet number  $Pe$ :

$$Pe = \frac{LU \rho_e c_p}{k_e},$$

we have the dimensionless energy conservation equation:

$$(\partial_t(\theta \rho(\phi)) + u \cdot \nabla(\theta \rho(\phi))) = \frac{1}{Pe} (k(\phi)(\partial_{xx}\theta + \partial_{yy}\theta)) + \frac{1}{\varepsilon^2 Pe} (k(\phi)\partial_{zz}\theta). \quad (2e)$$

The volume fraction conservation Eq. (1a) and the transport Eq. (1b) are left unchanged by this process. Henceforth, we consider that the flow is gravitational, so  $Fr^2 = \mathcal{O}(\varepsilon)$  and moreover that  $Re = \mathcal{O}(1)$  and  $Bi = \mathcal{O}(1)$  in  $\varepsilon$  and thus neglect the inertial term of the momentum equation. We also make the hypothesis that  $We = \mathcal{O}(\varepsilon^{-4})$  in order to neglect the surface tension term. In order to keep part of the temperature diffusion, we also assume that  $Pe = \mathcal{O}(\varepsilon^{-2})$ .

Using this set of equations, we reduce the tridimensional problem to a bidimensional one by reducing the equation to the 0th order in terms of  $\varepsilon$  and then by integrating along the vertical direction the equations. The process for obtaining the bidimensional equations solving  $h$  and  $\bar{\theta}$  is given in Bernabeu et al. (2016).

### 2.2.3. Dimensionless initial and boundary conditions

The initial and boundary conditions follow the same process of anisotropic dimensionless rewriting. The initial conditions and the Dirichlet conditions are left unchanged by this. After expanding the dot product with the outbound normal, the dimensionless free-surface condition on the Cauchy stress at  $z = h$  becomes:

$$-(\varepsilon^2 \tau_{xx} - p) \partial_x(h) - \varepsilon^2 \tau_{xy} \partial_y(h) + \tau_{xz} = 0 \quad (2f)$$

$$-\varepsilon^2 \tau_{xy} \partial_x(h) - (\varepsilon^2 \tau_{yy} - p) \partial_y(h) + \tau_{yz} = 0 \quad (2g)$$

$$-\varepsilon^2 \tau_{xz} \partial_x(h) - \varepsilon^2 \tau_{yz} \partial_y(h) + \varepsilon^2 \tau_{zz} + p = 0 \quad (2h)$$

The conductive heat transfer equation at the  $\Gamma_s$  boundary expresses as:

$$\begin{aligned} \varepsilon^2 (\partial_x(h) \partial_x(\theta|_{Q_f}) + \partial_y(h) \partial_y(\theta|_{Q_f})) - \partial_z(\theta|_{Q_f}) \\ = -\frac{k_s}{k} \varepsilon^2 (\partial_x(h) \partial_x(\theta|_{Q_s}) + \partial_y(h) \partial_y(\theta|_{Q_s})) - \partial_z(\theta|_{Q_s}) \end{aligned} \quad (2i)$$

and for  $\Gamma_e$ ,  $\theta = 1$ . The heat transfer condition at the free-surface  $\Gamma_f(t)$  yields:

$$-\varepsilon^2 (\partial_x(h) \partial_x(\theta) + \partial_y(h) \partial_y(\theta)) + \partial_z(\theta) + R p_\psi(\theta) \theta + Nu \theta = 0, \quad (2j)$$

where  $R = \frac{H \varepsilon \sigma_{SB} (\theta_e - \theta_a)^3}{k}$  a radiation number,  $Nu = \frac{\lambda H}{k}$  the Nusselt number,  $\psi = \frac{\theta_a}{\theta_e - \theta_a}$  a temperature ratio and  $p_\psi = (\theta)^3 + 4\psi(\theta)^2 + 6\psi^2(\theta) + 4\psi^3$  a polynomial used to linearize the radiation term.

### 2.2.4. Dimensionless heat transfer in the substrate

Considering purely vertical conduction in the substrate, we have in  $Q_s$ :

$$\partial_t \theta_s = Fo \partial_{zz} \theta_s \quad (2k)$$

with the Fourier number  $Fo = \frac{kT}{L^2}$  and the initial and boundary conditions:

$$\theta_s = \theta \text{ on } \Gamma_s \quad (2l)$$

$$\theta_s(z = -\infty) = 0 \quad (2m)$$

$$\theta_s(t = 0) = 0 \quad (2n)$$

According to Carslaw and Jaeger (1959, p. 58–64), this problem has a time-discrete solution, for all  $(x, y) \in \Omega$  and  $z < 0$ :

$$\theta(t_n, x, y, z) = \sum_{k=1}^n \theta(t_k, x, y, 0) \left[ \mathbb{I}_{]t_{k-1}, t_k[}(t_n) \left\{ 1 - \operatorname{erf} \left( \frac{z\sqrt{Fo}}{2\sqrt{(t_n - t_{k-1})}} \right) \right\} + \mathbb{I}_{]t_k, +\infty[}(t_n) \left\{ \operatorname{erf} \left( \frac{z\sqrt{Fo}}{2\sqrt{(t_n - t_k)}} \right) - \operatorname{erf} \left( \frac{z\sqrt{Fo}}{2\sqrt{(t_n - t_{k-1})}} \right) \right\} \right] \quad (2o)$$

where  $\mathbb{I}_S(\xi)$  denotes the indicator function, which is one when its argument  $\xi$  belongs to the set  $S$  and zero otherwise.

### 2.3. Bidimensional reduction

We rewrite the bidimensional reduced non-isotherm single-phase model from Bernabeu et al. (2016) by using the height-averaged volume fraction dependent parameters  $\rho(\bar{\phi})$ ,  $K(\bar{\theta}, \bar{\phi})$ ,  $\tau_y(\bar{\theta}, \bar{\phi})$  and  $k(\bar{\phi})$ . The model reduces to:

(P) Let  $\Omega$  be the bidimensional domain. Find  $h, \bar{\theta}$  and  $\bar{\phi}$  satisfying:

$$\partial_t h - \nabla_{2D}(\mu_n(K, B, h, \bar{\theta}, \bar{\phi}, |\nabla_{2D}h|)\nabla_{2D}h) = u_z(z=0) \text{ in } ]0; +\infty[ \times \Omega \quad (3a)$$

$$\mu_n = \begin{cases} \frac{n\rho(\bar{\phi})^{1/n}K(\bar{\theta}, \bar{\phi})^{-1/n}[(n+1)h\psi + nB(\bar{\theta}, \bar{\phi})][h\psi - B(\bar{\theta}, \bar{\phi})]^{(n+1)/n}}{(n+1)(2n+1)\psi^3} & \text{if } h\psi > B(\bar{\theta}, \bar{\phi}) \\ 0 & \text{otherwise.} \end{cases} \quad (3b)$$

$$h(t=0) = h_0 \text{ on } \Omega \quad (3c)$$

$$\frac{\partial h}{\partial \mathbf{n}} = 0 \text{ sur } ]0; +\infty[ \times \partial\Omega \quad (3d)$$

$$h(\partial_t \bar{\theta} + \bar{u}_{2D} \cdot \nabla \bar{\theta}) - u_z(z=0)(1 - \bar{\theta}) - \frac{k(\bar{\phi})}{\rho(\bar{\phi})Pe} [\partial_z \bar{\phi}] \bar{\theta} = 0 \text{ in } ]0; +\infty[ \times \Omega \quad (3e)$$

$$\bar{\theta}(t=0) = \bar{\theta}_0 \text{ sur } \Omega \quad (3f)$$

$$\frac{\partial \bar{\theta}}{\partial \mathbf{n}} = 0 \text{ sur } ]0; +\infty[ \times \partial\Omega \quad (3g)$$

$$\begin{cases} \bar{\varphi} = 1 \\ \partial_z \varphi + Rp_\mu(\bar{\theta}\varphi) + Nu\varphi = 0 \text{ sur } \Gamma_f(t) \\ -\partial_z \varphi + \frac{k_s}{k} \sqrt{\frac{Pe_s}{\pi t}} \varphi = 0 \text{ sur } \Gamma_s \text{ et } \bar{\theta}\varphi = 1 \text{ sur } \Gamma_e \\ \bar{\varphi}\bar{u}_{2D} = \bar{u}_{2D} \end{cases} \quad (3h)$$

$$\partial_t \bar{\phi} + \mathbf{u} \cdot \nabla \bar{\phi} + \nabla \cdot (\bar{\phi}(1 - \bar{\phi})\omega_z) = 0 \text{ in } ]0; +\infty[ \times Q(t) \quad (3i)$$

$$\bar{\phi}(t=0) = \bar{\phi}_0 \text{ in } Q(t) \quad (3j)$$

$$\bar{\phi} = 1 \text{ on } ]0; +\infty[ \times \Gamma_e \quad (3k)$$

$$\bar{\phi} = 0 \text{ on } ]0; +\infty[ \times \Gamma_s \quad (3l)$$

with  $u_{2D} = \begin{cases} \frac{n}{n+1} |\nabla_{2D}h|^{1/n} \rho(\bar{\phi})^{1/n} K(\bar{\theta}, \bar{\phi})^{-1/n} \frac{\nabla_{2D}h}{|\nabla_{2D}h|} [(h_c - z)^{(n+1)/n} - h_c^{(n+1)/n}] & \text{si } z \in [0; h_c[ \\ -\frac{n}{n+1} |\nabla_{2D}h|^{1/n} \rho(\bar{\phi})^{1/n} K(\bar{\theta}, \bar{\phi})^{-1/n} \frac{\nabla_{2D}h}{|\nabla_{2D}h|} h_c^{(n+1)/n} & \text{si } z \in [h_c; h], \end{cases}$  and the

plug height  $h_c(t, x, y) = \max \left( 0, h - \frac{B(\bar{\theta}, \bar{\phi})}{\rho(\bar{\phi})|\nabla_{2D}h|} \right)$ . The subscript  $_{2D}$  denotes the vectors in the  $(0xy)$  planes, such that  $\mathbf{u}_{2D} = (u_x, u_y)$ .

It remains to reduce the equations on the volume fraction (3i)–(3l) as they are still defined in the tridimensional domain  $Q(t)$ . Integrating Eq. (3i) and using the mass conservation Eq. (2b) and the transport Eq. (3a), we have:

$$h\partial_t \bar{\phi} + \nabla_{2D}(h\bar{\phi}\bar{u}_{2D}) - \nabla_{2D}(h\bar{u}_{2D})\bar{\phi} + u_z(z=0)(\bar{\phi} - \phi(z=0)) + [(1 - \phi)\bar{\phi}\omega_z]_0^h = 0 \quad (3m)$$

In order to have a fully bidimensional equation in  $\bar{\phi}$ , we follow the process used by Bernabeu et al. (2016) for the vertical distribution of  $\theta$  for the volume fraction by introducing a similar unknown function

$\zeta$  satisfying  $\bar{\zeta} = 1$  and  $\bar{\zeta}\bar{u}_{2D} = \bar{u}_{2D}$  chosen so that  $\phi(t, x, y, z) = \zeta(t, x, y, z)\bar{\phi}(t, x, y)$ . With this notation, the boundary conditions become:

$$\zeta(z=0)\bar{\phi} = 1 \text{ on } \Gamma_e \quad (3n)$$

$$\zeta(z=0)\bar{\phi} = 0 \text{ on } \Gamma_s \quad (3o)$$

Assuming that due to high viscosity and density of the continuous phase, the gas will remain stuck towards the bottom of the spread and transported, thus we apply a polynomial first order by parts for its vertical distribution:

$$\zeta(t, x, y, z) = \begin{cases} az + b & \text{for } z \in [0; z_c[ \\ \frac{1}{\bar{\phi}} & \text{for } z \in [z_c; h]. \end{cases} \quad (3p)$$

Where  $z_c$  is the height below which there is a two phase mixture.

Finally, the multiphase bidimensional reduced problem is obtained by replacing in (P) Eq. (3i)–(3l) by:

$$h(\partial_t \bar{\phi} + \bar{u}_{2D} \cdot \nabla_{2D}(\bar{\phi})) + u_z(0)\bar{\phi}(1 - \zeta(0)) + [(1 - \bar{\phi}\zeta)\bar{\phi}\zeta\omega_z]_0^h = 0 \text{ in } ]0; +\infty[ \times \Omega \quad (3q)$$

$$\bar{\phi}(t=0) = \bar{\phi}_{init} \text{ on } \Omega \quad (3r)$$

$$\frac{\partial \bar{\phi}}{\partial \mathbf{n}} = 0 \text{ on } ]0; +\infty[ \times \partial\Omega \quad (3s)$$

As shown in Bernabeu et al. (2016), ignoring the conditions on the vertical profiles  $\bar{\zeta}\bar{u}_{2D} = \bar{u}_{2D}$  and  $\bar{\varphi}\bar{u}_{2D} = \bar{u}_{2D}$  to simplify their expressions yields acceptable error, thus here we use respectively first order by parts and second order polynomials.

### 2.4. Numerical resolution

Firstly, the problem (P) is discretized versus time using a implicit second-order variable step finite difference scheme (BFD2) as in Bernabeu et al. (2014, 2016), Schiano et al. (2023). At each time step, an under-relaxed fixed point algorithm is used to solve the nonlinear subproblems in  $h, \bar{\theta}$  and  $\bar{\phi}$ . Finally, these equations are spatially discretized using a finite element method based on the C++ library Rheolef (Saramito, 2019) on a rectangular geometry (see Fig. 3). We use the adaptive meshing option this library provides based on the BAMG code (Hecht, 2006) by refining the mesh around the front of the flow, where our variables gradients are the greatest.

For the inlet velocity  $u_z(z=0)$ , we use a spatial distribution so that it annuls around the line  $x=0$ , where the vertical boundary conditions on  $\varphi$  and  $\zeta$  change, in order to reduce numerical instabilities. For the region  $x > 0$ , corresponding to where degassing takes place, we consider that gas is provided from the substrate due to energy transfer from the melt, thus  $u_z(t, x > 0, y, z=0) > 0$  only if the melt is present ( $h(t, x, y) > 0$ ).

To prevent numerical instabilities around  $x=0$ , the boundary conditions (3n) and (3o) have been modified around the line  $x=0$  by instead using the following continuous boundary condition:

$$\bar{\phi}(z=0) = f(x)|_{x_c} = \frac{1}{2} \operatorname{erfc}(x/x_c). \quad (4a)$$

In the region  $-x_c < x < x_c$ , the first order polynomial by parts vertical distribution  $\zeta(t, x, y, z)$  becomes:

$$\zeta = \begin{cases} az + \frac{f_{x_c}(x)}{\bar{\phi}} & \text{for } z \in [0; z_c[ \\ b = \frac{1}{\bar{\phi}} & \text{for } z \in [z_c; h] \end{cases} \quad (4b)$$

using the same conditions on  $\zeta$  as in the system (3p), we obtain:

$$\begin{cases} a = \frac{1}{z_c\bar{\phi}}(1 - f_{x_c}(x)) \\ b = \frac{1}{\bar{\phi}} \end{cases} \quad (4c)$$

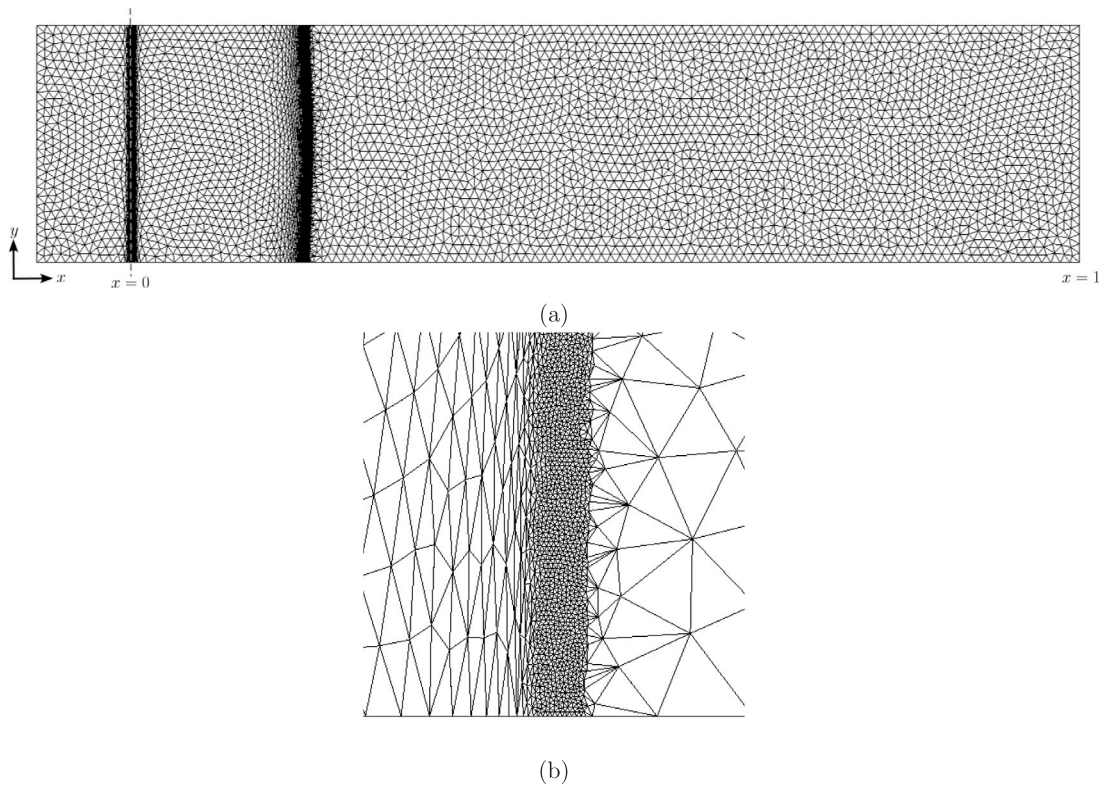


Fig. 3. (a) Auto-generated mesh and (b) Zoom of mesh (a) at the front of the spread.

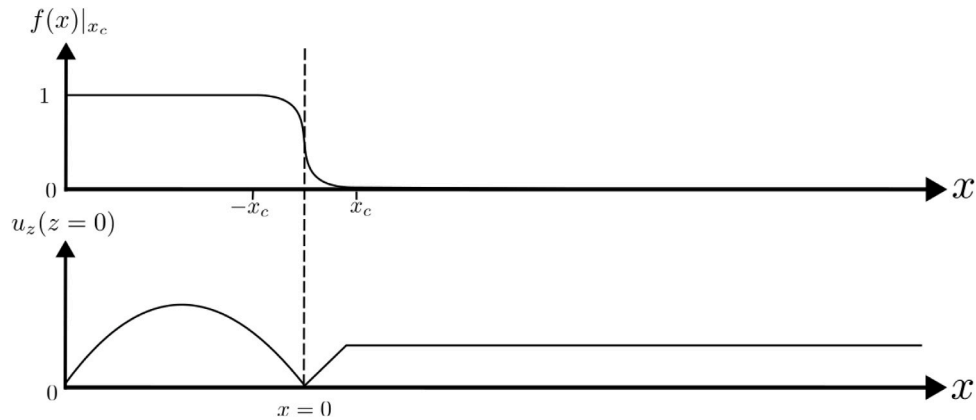


Fig. 4. Spatial distribution for the inlet condition  $u_z(z=0)$  and the boundary smoothing function  $f(x)|_{x_c}$ .

By replacing  $w_z$  and  $\zeta$  by their values in Eq. (3q), we have the following equation that is implemented in our simulation:

$$h(\partial\bar{\phi} + \zeta\bar{u}_{2D} \cdot \nabla_{2D}(\bar{\phi})) + u_z(0)\bar{\phi}\left(1 - \frac{f_{x_c}(x)}{\bar{\phi}}\right) - \frac{c_0}{c_f}(1 - f_{x_c}(x))^2\bar{\phi}f_{x_c}^2(x) = 0 \quad (4d)$$

Those two numerical approximations are depicted on Fig. 4.

### 3. Application to corium

We apply this model to a case based on the VEU7 corium spreading experiment (Journeau et al., 2006) with a simplified geometry, corium being the material produced by melting nuclear power plants core and their surroundings in severe accidents. We use the geometry depicted on Fig. 3, and material properties issued from previous studies on corium spreading, such as Roche et al. (1994), Ramacciotti et al. (2001), Journeau et al. (2006), Chawla et al. (1981). The volumetric melt flow rate of the melt is  $8.4 \cdot 10^{-4} \text{ m}^3 \text{ s}^{-1}$  (Journeau et al., 2006)

during 5 s, with  $t = 0$  s corresponding to the start of inlet feeding. As argued in Schiano et al. (2023), this experiment could be modeled using the previous equations for the single phase case, here we aim to observe the influence of degassing on spreading, as it was observed on the experiment as described in Journeau et al. (2003). Thereafter, Tables 1 and 2 present the main flow and material properties of the VEU7 spreading test. Dimensionless parameters using these are computed in Table 3, characterizing the flow regimes, enabling the use of the preceding model. The high value of Weber number confirms here that we can neglect the surface tension forces in this application.

### 4. Results and discussion

#### 4.1. Numerical convergence analysis

We first perform a sensitivity analysis on numerical parameters: the time step  $dt$ , the minimal mesh size  $h_{min}$ , to ensure proper temporal

**Table 1**

Flow properties of the VEU7 corium spreading test (Journeau et al., 2003; Roche et al., 1994; Ramacciotti et al., 2001; Journeau et al., 2006; Wittmaack, 2002; Journeau et al., 1999; Sudreau and Cognet, 1997; Piluso et al., 2002).

Quantity	Symbol	Corium
Characteristic height m	$H$	$6.5 \cdot 10^{-2}$
Characteristic length m	$L$	$4.0 \cdot 10^{-1}$
Aspect ratio	$\varepsilon = \frac{H}{L}$	0.15
Characteristic velocity m s <sup>-1</sup>	$U$	1.53
Inlet fluid temperature K	$\theta_e$	2450
Initial substrate and air temperature K	$\theta_a$	303

**Table 2**

Material properties of the VEU7 corium spreading test (Journeau et al., 2003; Roche et al., 1994; Ramacciotti et al., 2001; Journeau et al., 2006; Wittmaack, 2002; Journeau et al., 1999; Sudreau and Cognet, 1997; Piluso et al., 2002).

Quantity	Symbol	Corium
Spread density (kg m <sup>-3</sup> )	$\rho_1$	7500
Air density (kg m <sup>-3</sup> )	$\rho_2$	1.2
Dynamic viscosity at temperature $\theta_e$ (Pa s)	$K_e$	$2.24 \cdot 10^1$
Yield stress at temperature $\theta_e$ (Pa)	$\tau_{y,e}$	$10^2$
Emissivity (-)	$\varepsilon$	0.8
Thermal conductivity (W m <sup>-1</sup> K <sup>-1</sup> )	$k$	3
Specific heat (J kg <sup>-1</sup> K <sup>-1</sup> )	$c_p$	995.6
Convective heat transfer coefficient with air (W m <sup>-2</sup> K <sup>-1</sup> )	$\lambda$	300
Surface tension (N m <sup>-1</sup> )	$\sigma_{cap}$	0.58

**Table 3**

Dimensionless parameters for experiment VEU7.

	VEU7
Froude = $\frac{U}{\sqrt{gL}}$	$7.06 \cdot 10^{-1}$
Reynolds = $\frac{\rho_1 U L}{K_e}$	$1.40 \cdot 10^2$
Weber = $\frac{\rho_1 U^2 L}{K_e}$	$9.79 \cdot 10^3$
Péclet = $\frac{LU\sigma_{cap}}{k_e}$	$1.69 \cdot 10^5$

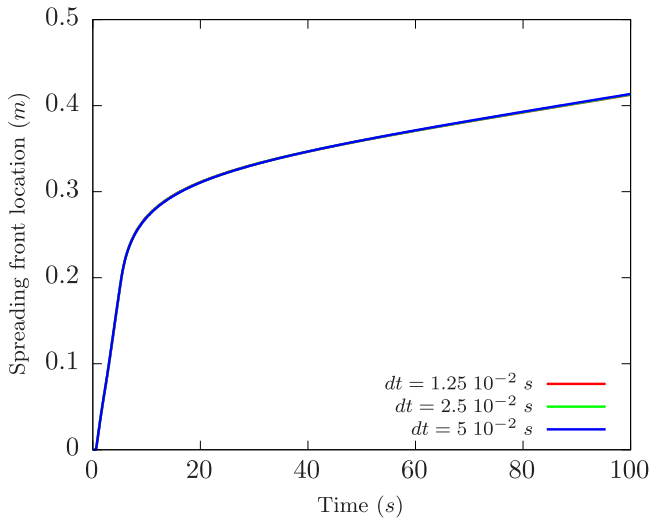


**Fig. 5.** Simulated front progress for  $Arr = 7.10^{-3}$ ,  $\tau_y = 200$  Pa,  $n = 0.66$ ,  $hmin = 5.10^{-4}$  m, a degassing velocity of  $u_z(z = 0) = 10^{-4}$  m s<sup>-1</sup> and different values of time step.

and spatial convergence and the aforementioned smoothing parameter  $x_c$  around  $x = 0$  for  $\phi$  boundary condition. Fig. 5 shows that computation is sufficiently resolved in terms of time step, we thus use the value  $dt = 5.10^{-2}$  s to reduce computation time.

The parameter  $hmin$  is given in the adaptive meshing routine: it gives a lower limit to mesh size. We observe on Fig. 6 that the convergence using this parameter is non linear and that a value of

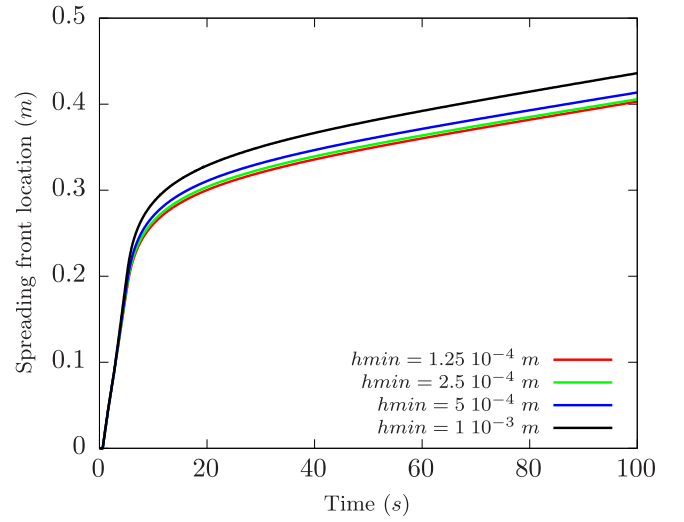


**Fig. 6.** Simulated front progress for  $Arr = 7.10^{-3}$ ,  $\tau_y = 200$  Pa,  $n = 0.66$ ,  $dt = 5.10^{-2}$  m, a degassing velocity of  $u_z(z = 0) = 10^{-4}$  m s<sup>-1</sup> and different values of minimal mesh size.

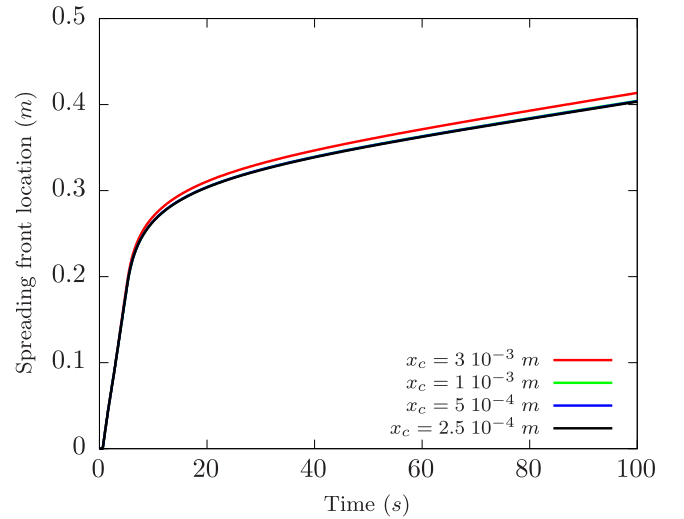


**Fig. 7.** Simulated front progress for  $Arr = 7.10^{-3}$ ,  $\tau_y = 200$  Pa,  $n = 0.66$ , a degassing velocity of  $u_z(z = 0) = 10^{-4}$  m s<sup>-1</sup> and different values of lower volume fraction boundary condition transition region size  $x_c$ .

$hmin \leq 5 \cdot 10^{-4}$  m is a good compromise in terms of convergence and computation time.

We then conduct a sensitivity analysis on the numerical parameter  $x_c$  from Eq. (4a), corresponding to the size of the transition region between the boundary conditions on  $\phi(z = 0)$ . No difference is found for  $x_c < 1.10^{-3}$  m as seen on Fig. 7. We will thus use these values for further computations.

#### 4.2. 3D visualization of velocity and volume fraction

Using the expression of  $u_{2D}$  and the mass conservation equation, we can depict the tridimensional velocity field, as in Fig. 8. Fig. 8(a) shows this 3D representation without the inlet velocity and with the height-average volume fraction of the melt  $\bar{\phi}$  on the free-surface at a snapshot during the spreading. From these two results, profiles at different time steps are given on Figs. 8(b–d): the maximum velocity corresponds at every time step with a local minimum in gas fraction, indicating that it has been locally transported to the front of the spread, as seen by the subsequent local maximum. This explains in part the

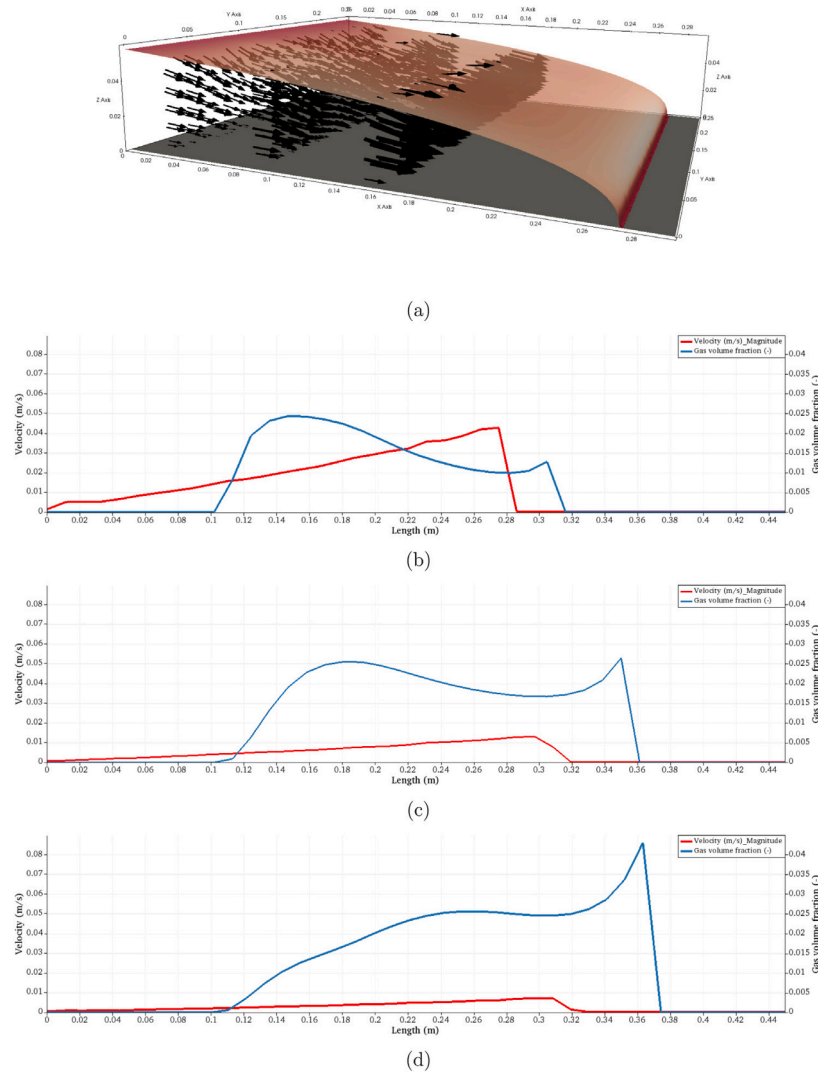


Fig. 8. (a) 3D reconstruction of the velocity field. The upper surface represents  $\bar{\phi}$  and (b-d)  $1 - \bar{\phi}$  the height-averaged gas volume fraction and  $|\mathbf{u}|$  along the  $x$ -axis for (b)  $t = 5.5$  s (c)  $t = 7.5$  s and (d)  $t = 9.65$  s for  $u_z(z = 0) = 10^{-4}$  m s $^{-1}$ . The velocity norm is taken at  $y = 0.125$  m and  $z = 0.03$  m.

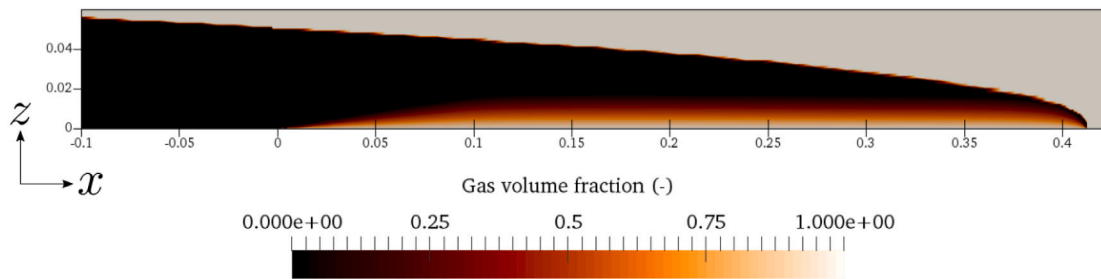


Fig. 9. Gas volume fraction distribution for  $y = 0.125$  m at  $t = 100$  s for  $Arr = 7.10^{-3}$ ,  $\tau_y = 200$  Pa,  $n = 0.66$ , and  $u_z(z = 0) = 10^{-4}$  m s $^{-1}$ .

observation on Fig. 9 that at the end of the simulation, there is more gas fraction towards the front. We can also remark on this figure that at the leading edge of the spread, we have  $\phi = 1$ , which is due to the lack of degassing boundary condition to our model at the free surface and vertical distribution of volume fraction used. Using the temperature vertical distribution  $\phi$ , we can compute the tridimensional temperature field by definition  $\theta(x, y, z, t) = \bar{\theta}(x, y, t)\phi(x, y, z, t)$ . Fig. 10 shows limited

internal cooling of the flow, with is coherent with the large Peclet number.

### 4.3. Sensitivity analysis

Fig. 11 compares the single phase case with the multiphase one, showing a greater velocity before reaching the viscoplastic regime



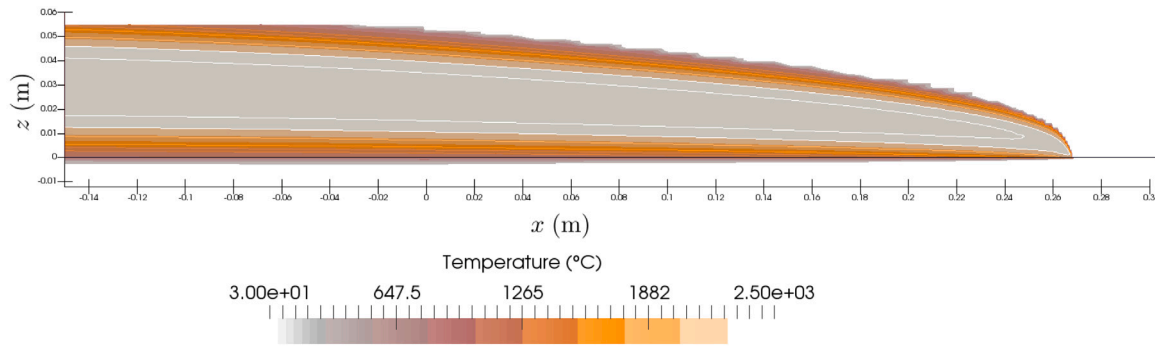


Fig. 10. Temperature at  $y = 10$  cm and  $t = 5$  s, in both the flow and the substrate.

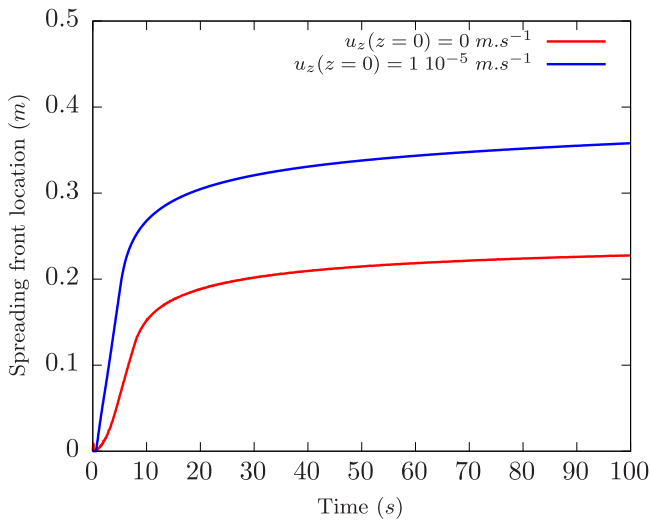


Fig. 11. Simulated front progress for  $Arr = 7.10^{-3}$ ,  $\tau_y = 200$  Pa,  $n = 0.66$ ,  $u_z(z = 0) = 1 \cdot 10^{-5}$  m s $^{-1}$  and no degassing.

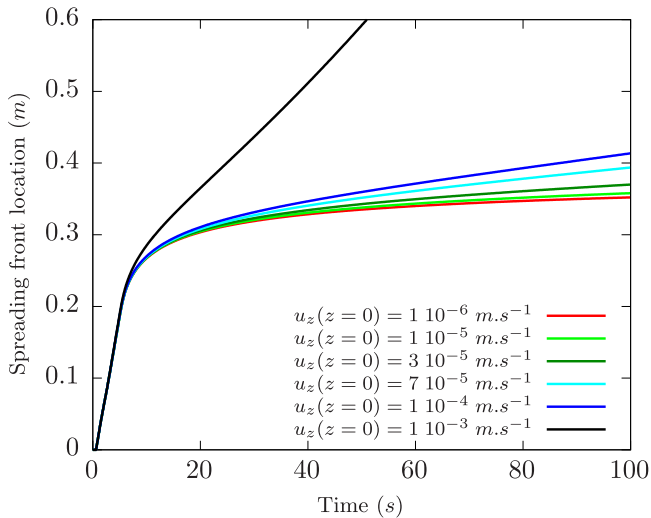


Fig. 12. Simulated front progress for  $Arr = 7.10^{-3}$ ,  $\tau_y = 200$  Pa,  $n = 0.66$ , and different degassing velocities  $u_z(z = 0)$ .

around  $t = 10$  s characterized by the curve inflexion. Since the gas distribution described by  $\zeta$  confines the gas to the lower parts of the medium, we expect the dynamic to be similar to that of a fluidized bed, though the equations solved are height-averaged. A non averaged approach would probably see greater differences between the two cases. The lack of agitation model by the bubble in the flow as described

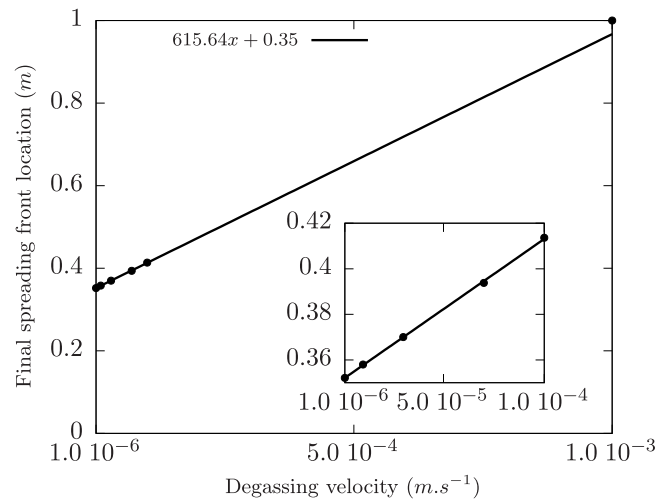


Fig. 13. Front position at  $t = 100$  s for  $Arr = 7.10^{-3}$ ,  $\tau_y = 200$  Pa,  $n = 0.66$ , and different degassing velocities  $u_z(z = 0)$ . The continuous line is a linear regression of the points for  $1.10^{-6} \leq u_z(z = 0) \leq 1.10^{-4}$  with  $R^2 = 0.9996$ .

in Jubaidah et al. (2020) is also coherent with this observation. Such a model would increase the effective viscosity and slow down the spreading.

Sensitivity analysis on the degassing velocity  $u_z(z = 0)$  results are shown on Fig. 12. During the melt feeding period ( $t < 5$  s), gas addition seems to have little influence, due to higher momentum from the melt than the gas and the low proportion of the latter as it has yet to reach the degassing surface. To quantify the nature of the influence of degassing velocity on final spreading length, we performed a linear regression shown on Fig. 13. We found a linear relation between them, with a coefficient of determination  $R^2 > 0.999$ , for the range  $10^{-6} \text{ m s}^{-1} \leq u_z(z = 0)|_{h>0} \leq 10^{-4} \text{ m s}^{-1}$ . For higher degassing velocities, the added gas stress surpasses the yield stress, enabling further spread and an increase in degassing surface, corresponding to a non-linear behavior.

Gas volume fraction  $(1 - \bar{\phi})$  behaves almost linearly with respect to time for degassing velocities  $u_z(z = 0) < 3.10^{-5} \text{ m s}^{-1}$  after melt inlet feeding as shown on Fig. 14. In this condition, the added stress from the gas is not enough to surpass yield stress. Consequently, the degassing surface remains constant when the flow is stopped, explaining the linear progression of gas volume fraction. For higher degassing velocities such as  $u_z(z = 0) = 1.10^{-3} \text{ m s}^{-1}$ , this behavior is non linear as added stress from the gas is higher than the yield stress, increasing the degassing surface by preventing stoppage. Zoom on Fig. 14 indicates clearly the influence from the boundary condition smoothing function Eq. (4a): gas volume fraction rises both due to the spread progressing on the degassing substrate, and due to a source of a mix of melt and gas in the region  $-x_c < x < x_c$ .

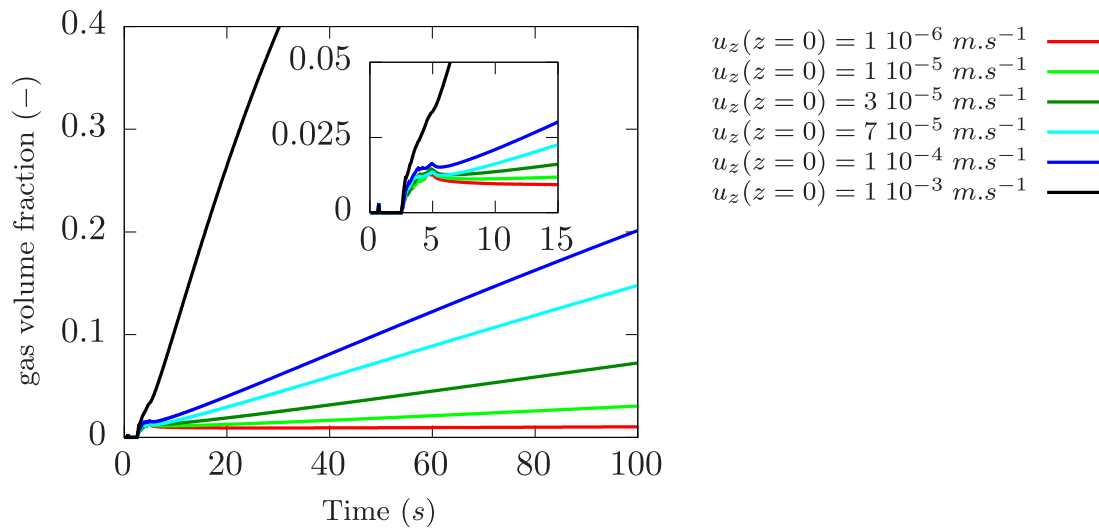


Fig. 14. Simulated gas volume fraction for  $Arr = 7.10^{-3}$ ,  $\tau_y = 200$  Pa,  $n = 0.66$ , and different degassing velocities  $u_z(z=0)$  and zoom at the beginning of the spread.

## 5. Conclusions

A new asymptotic model for free surface multiphase viscoplastic anisotherm flows has been presented, based on the single phase anisotherm model developed by Bernabeu et al. (2016). A sensitivity analysis has been conducted on the numerical parameters and the amount of gas injected in the mixture that is spreading over a surface. A tridimensional representation of velocity and species volume fraction has been computed respectively from an explicit solution and an arbitrary vertical distribution with the result found to be coherent with the theory. Future work include the use of more representative vertical boundary conditions for the volume fraction, notably to enable gas release at the free-surface and to provide better quantitative degassing rate through a phase change model of the substrate and a germination model for the gas at the interface between the mixture and the substrate, which would change the vertical volume fraction distribution. The model also could be improved by removing the hypothesis that there is thermal equilibrium between the phases. Further developments on the modeling of free surface flows for nuclear safety would be to include chemical description to the model to take into account molten core-concrete interaction (such as substrate ablation), and inertial regime turbulence description to describe large scale accidents in nuclear power plants.

## CRedit authorship contribution statement

**Thomas Schiano:** Conceptualization, Methodology/Study design, Software, Validation, Formal analysis, Investigation, Writing – original draft, Writing – review & editing, Visualization. **Barbara Bigot:** Conceptualization, Methodology/Study design, Formal analysis, Investigation, Resources, Writing – review & editing, Project administration, Funding acquisition. **Jean-François Haquet:** Conceptualization, Methodology/Study design, Investigation, Writing – review & editing, Project administration, Funding acquisition. **Pierre Saramito:** Conceptualization, Software, Resources, Writing – review & editing, Project administration. **Claude Smutek:** Conceptualization, Investigation, Writing – review & editing.

## Declaration of competing interest

The authors declare that they have no known competing financial interests or personal relationships that could have appeared to influence the work reported in this paper.

## Data availability

Data will be made available on request.

## References

- Allen, S.M., Cahn, J.W., 1979. A microscopic theory for antiphase boundary motion and its application to antiphase domain coarsening. *Acta Metall.* 27 (6), 1085–1095. [http://dx.doi.org/10.1016/0001-6160\(79\)90196-2](http://dx.doi.org/10.1016/0001-6160(79)90196-2), URL <https://linkinghub.elsevier.com/retrieve/pii/0001616079901962>.
- Balmforth, N., Craster, R., Perona, P., Rust, A., Sassi, R., 2007. Viscoplastic dam breaks and the Bostwick consistometer. *J. Non-Newton. Fluid Mech.* 142 (1–3), 63–78. <http://dx.doi.org/10.1016/j.jnnfm.2006.06.005>, URL <https://linkinghub.elsevier.com/retrieve/pii/S0377025706001613>.
- Balmforth, N.J., Craster, R.V., Sassi, R., 2004. Dynamics of cooling viscoplastic domes. *J. Fluid Mech.* 499, 149–182. <http://dx.doi.org/10.1017/S0022112003006840>, URL [http://www.journals.cambridge.org/abstract\\_S0022112003006840](http://www.journals.cambridge.org/abstract_S0022112003006840).
- Bercovici, D., Lin, J., 1996. A gravity current model of cooling mantle plume heads with temperature-dependent buoyancy and viscosity. *J. Geophys. Res. Solid Earth* 101 (B2), 3291–3309. <http://dx.doi.org/10.1029/95JB03538>, URL <http://doi.wiley.com/10.1029/95JB03538>.
- Bernabeu, N., Saramito, P., Smutek, C., 2014. Numerical modeling of non-Newtonian viscoplastic flows: Part II. Viscoplastic fluids and general tridimensional topographies. *Int. J. Numer. Anal. Model.* 11 (1), 213–228.
- Bernabeu, N., Saramito, P., Smutek, C., 2016. Modelling lava flow advance using a shallow-depth approximation for three-dimensional cooling of viscoplastic flows. *Geol. Soc. Lond. Special Publ.* 426 (1), 409–423. <http://dx.doi.org/10.1144/SP426.27>, URL <http://sp.lyellcollection.org/lookup/doi/10.1144/SP426.27>.
- Bingham, E.C., 1922. *Fluidity and Plasticity*. Mc Graw-Hill, New-York, USA, <http://www.archive.org/download/fluidityandplast007721mbp/fluidityandplast007721mbp.pdf>.
- Brackbill, J., Kothe, D., Zemach, C., 1992. A continuum method for modeling surface tension. *J. Comput. Phys.* 100, 335–354.
- Cahn, J.W., Hilliard, J.E., 1958. Free energy of a nonuniform system. I. Interfacial free energy. *J. Chem. Phys.* 28 (5), 258–267.
- Carslaw, H.S., Jaeger, J.C., 1959. *Conduction of Heat in Solids*. Oxford University Press.
- Chawla, T., Graff, D., Borg, R., Bordner, G., Weber, D., Miller, D., 1981. Thermophysical properties of mixed oxide fuel and stainless steel type 316 for use in transition phase analysis. *Nucl. Eng. Des.* 67 (1), 57–74. [http://dx.doi.org/10.1016/0029-5493\(81\)90155-2](http://dx.doi.org/10.1016/0029-5493(81)90155-2), URL <https://linkinghub.elsevier.com/retrieve/pii/0029549381901552>.
- Chiu, P.-H., 2011. A conservative phase field method for solving incompressible two-phase flows. *J. Comput. Phys.* 20.
- Damián, S.M., Nigro, N.M., 2014. An extended mixture model for the simultaneous treatment of small-scale and large-scale interfaces: An extended mixture model for small-scale and large-scale interfaces. *Internat. J. Numer. Methods Fluids* 75 (8), 547–574. <http://dx.doi.org/10.1002/fld.3906>, URL <https://onlinelibrary.wiley.com/doi/10.1002/fld.3906>.
- Hecht, F., 2006. BAMG: bidimensional anisotropic mesh generator. <https://www.ljll.math.upmc.fr/hecht/ftp/bamg>.
- Herschel, W.H., Bulkley, T., 1926. Measurement of consistency as applied to rubber-benzene solutions. *Proc. Am. Soc. Test. Mater.* 26 (2), 621–633.

- Hibiki, T., Ishii, M., 2003. One-dimensional drift-flux model for two-phase flow in a large diameter pipe. *Int. J. Heat Mass Transfer* 46 (10), 1773–1790. [http://dx.doi.org/10.1016/S0017-9310\(02\)00473-8](http://dx.doi.org/10.1016/S0017-9310(02)00473-8), URL <https://linkinghub.elsevier.com/retrieve/pii/S0017931002004738>.
- Huppert, H.E., 1982. The propagation of two-dimensional and axisymmetric viscous gravity currents over a rigid horizontal surface. *J. Fluid Mech.* 121 (-1), 43. <http://dx.doi.org/10.1017/S0022112082001797>.
- Ishii, M., 1977. One-Dimensional Drift-Flux Model and Constitutive Equations for Relative Motion Between Phases in Various Two-Phase Flow Regimes. *Tech. Rep. ANL-77-47*, Argonne National Laboratory.
- Ishii, M., Zuber, N., 1979. Drag coefficient and relative velocity in bubbly, droplet or particulate flows. *AIChE J.* 25 (5), 843–855. <http://dx.doi.org/10.1002/aic.690250513>, URL <https://onlinelibrary.wiley.com/doi/10.1002/aic.690250513>.
- Journeau, C., Boccaccio, E., Brayer, C., Cognet, G., Haquet, J.-F., Jégou, C., Piluso, P., Moneris, J., 2003. Ex-vessel corium spreading: results from the VULCANO spreading tests. *Nucl. Eng. Des.* 223 (1), 75–102. [http://dx.doi.org/10.1016/S0029-5493\(02\)00397-7](http://dx.doi.org/10.1016/S0029-5493(02)00397-7), URL <https://linkinghub.elsevier.com/retrieve/pii/S0029549302003977>.
- Journeau, C., Haquet, J.-F., Spindler, B., Spengler, C., Foit, J., 2006. The Vulcano VE-U7 Corium spreading benchmark. *Prog. Nucl. Energy* 48 (3), 215–234. <http://dx.doi.org/10.1016/j.pnucene.2005.09.009>, URL <https://linkinghub.elsevier.com/retrieve/pii/S0149197005001782>.
- Journeau, C., Sudreau, F., Gatt, J.-M., Cognet, G., 1999. Thermal, physico-chemical and rheological boundary layers in multi-component oxidic melt spreads. *Int. J. Therm. Sci.* 38 (10), 879–891. [http://dx.doi.org/10.1016/S1290-0729\(99\)80042-8](http://dx.doi.org/10.1016/S1290-0729(99)80042-8), URL <https://linkinghub.elsevier.com/retrieve/pii/S1290072999800428>.
- Jubaidah, Duan, G., Yamaji, A., Journeau, C., Buffe, L., Haquet, J.-F., 2020. Investigation on corium spreading over ceramic and concrete substrates in VULCANO VE-U7 experiment with moving particle semi-implicit method. *Ann. Nucl. Energy* 141, 107266. <http://dx.doi.org/10.1016/j.anucene.2019.107266>, URL <https://linkinghub.elsevier.com/retrieve/pii/S0306454919307765>.
- Liu, K.F., Mei, C.C., 1989. Slow spreading of a sheet of Bingham fluid on an inclined plane. p. 25.
- Meng, W., Liao, L., Chen, M., Yu, C.-h., Li, J., An, R., 2022. An enhanced CLSVOF method with an algebraic second-reconstruction step for simulating incompressible two-phase flows. *Int. J. Multiph. Flow.* 154, 104151. <http://dx.doi.org/10.1016/j.ijmultiphaseflow.2022.104151>, URL <https://linkinghub.elsevier.com/retrieve/pii/S0301932222001422>.
- Piluso, P., Moneris, J., Journeau, C., Cognet, G., 2002. Viscosity measurements of ceramic oxides by aerodynamic levitation. *Int. J. Thermophys.* 23 (5), 1229–1240.
- Ramacciotti, M., Journeau, C., Sudreau, F., Cognet, G., 2001. Viscosity models for corium melts. *Nucl. Eng. Des.* 204 (1–3), 377–389. [http://dx.doi.org/10.1016/S0029-5493\(00\)00328-9](http://dx.doi.org/10.1016/S0029-5493(00)00328-9), URL <https://linkinghub.elsevier.com/retrieve/pii/S0029549300003289>.
- Roche, M., Steidl, D., Leibowitz, L., Fink, J., Raj Sehgal, B., 1994. Viscosity of Corium-Concrete Mixtures at High Temperatures. *Argonne National Laboratory Report ACE-TR-C37*, Argonne National Laboratory, ANL, p. 90.
- Roult, G., Peltier, A., Taisne, B., Staudacher, T., Ferrazzini, V., Di Muro, A., 2012. A new comprehensive classification of the Piton de la Fournaise activity spanning the 1985–2010 period. Search and analysis of short-term precursors from a broadband seismological station. *J. Volcanol. Geotherm. Res.* 241–242, 78–104. <http://dx.doi.org/10.1016/j.jvolgeores.2012.06.012>, URL <https://linkinghub.elsevier.com/retrieve/pii/S0377027312001801>.
- Saramito, P., 2019. Rheolef 7.1, an efficient C++ finite element environment. URL <https://www-ljk.imag.fr/membres/Pierre.Saramito/rheolef/html/index.html>.
- Saramito, P., Wachs, A., 2017. Progress in numerical simulation of yield stress fluid flows. *Rheol. Acta* 56 (3), 211–230. <http://dx.doi.org/10.1007/s00397-016-0985-9>, URL <http://link.springer.com/10.1007/s00397-016-0985-9>.
- Schiano, T., Bigot, B., Haquet, J.-F., Saramito, P., Smutek, C., 2023. A viscoplastic approach to corium spreading during a severe nuclear accident. *Nuc. Eng. Des.* 401, 112045. <http://dx.doi.org/10.1016/j.nucengdes.2022.112045>, <https://www.sciencedirect.com/science/article/pii/S002954932200396X>.
- Shaw, H.R., 1969. Rheology of Basalt in the Melting Range. *J. Petrol.* 10 (3), 510–535. <http://dx.doi.org/10.1093/petrology/10.3.510>, URL <https://academic.oup.com/petrology/article-lookup/doi/10.1093/petrology/10.3.510>.
- Sudreau, F., Cognet, G., 1997. Corium viscosity modelling above liquidus temperature. *Nucl. Eng. Des.* 178 (3), 269–277. [http://dx.doi.org/10.1016/S0029-5493\(97\)00137-4](http://dx.doi.org/10.1016/S0029-5493(97)00137-4), URL <https://linkinghub.elsevier.com/retrieve/pii/S0029549397001374>.
- Villeneuve, N., Neuville, D.R., Boivin, P., Bachèlery, P., Richet, P., 2008. Magma crystallization and viscosity: A study of molten basalts from the Piton de la Fournaise volcano (La Réunion Island). *Chem. Geol.* 256 (3–4), 242–251. <http://dx.doi.org/10.1016/j.chemgeo.2008.06.039>, URL <https://linkinghub.elsevier.com/retrieve/pii/S0009254108002635>.
- Weisshäupl, H., 1999. Severe accident mitigation concept of the EPR. *Nucl. Eng. Des.* 187 (1), 35–45. [http://dx.doi.org/10.1016/S0029-5493\(98\)00256-8](http://dx.doi.org/10.1016/S0029-5493(98)00256-8), URL <https://linkinghub.elsevier.com/retrieve/pii/S0029549398002568>.
- Wittmaack, R., 2002. Simulation of free-surface flows with heat transfer and phase transitions and application to corium spreading in the EPR. *Nucl. Technol.* 137 (3), 194–212. <http://dx.doi.org/10.13182/NT02-A3268>, URL <https://www.tandfonline.com/doi/full/10.13182/NT02-A3268>.